Joint inversion of daily and long-period geomagnetic variations reveals lateral variations in upper mantle and transition zone water content

Federico Daniel Munch[1], Alexander V Grayver[1], Martina Guzavina[2], Alexey Kuvshinov[3], and Amir Khan[4]

[1]Insitute of Geophysics, ETH Zürich
[2]Institute of Geophysics, ETH Zurich
[3]Institute of Geophysics
[4]Swiss Federal Institute of Technology

November 22, 2022

Abstract

We present a novel approach to investigate variations in upper mantle and transition zone (MTZ) water content based on the joint analysis of electromagnetic (EM) signals originating in the ionosphere and magnetosphere. We inverted EM signals (period range 6 hours–85 days) to probe the electrical conductivity structure underneath 20 geomagnetic observatories, accounting for the complex spatial structure of the ionospheric and magnetospheric sources. The joint inversion of EM data for the daily and long-period bands led to a significantly improved model resolution in the upper mantle and MTZ. The conductivity profiles reveal significant lateral variability, which we interpreted in terms of upper mantle and MTZ water content by a stochastic coupling of electrical conductivity with constrains on the mantle thermo-chemical structure derived from the analysis of seismic data. Our results suggest the existence of a relatively dry MTZ beneath Europe and a water-enriched MTZ underneath North America and northern Asia.

Joint inversion of daily and long-period geomagnetic variations reveals lateral variations in upper mantle and transition zone water content

F. D. Munch[1], **A. V. Grayver**[1], **M. Guzavina**[1], **A. V. Kuvshinov**[1], **A. Khan**[1,2]

[1]Institute of Geophysics, ETH Zurich, Switzerland
[2]Institute of Theoretical Physics, University of Zurich, Switzerland.

Key Points:

- Joint inversion of daily and long-period geomagnetic variations results in better resolved mantle conductivity structure
- Incorporation of seismic constraints helps isolate mantle water content
- We find a relatively dry mantle beneath Europe and a water-enriched transition zone underneath North America and northern Asia

Corresponding author: Federico D. Munch, federico.munch@erdw.ethz.ch

Abstract

We present a novel approach to investigate variations in upper mantle and transition zone (MTZ) water content based on the joint analysis of electromagnetic (EM) signals originating in the ionosphere and magnetosphere. We inverted EM signals (period range 6 hours–85 days) to probe the electrical conductivity structure underneath 20 geomagnetic observatories, accounting for the complex spatial structure of the ionospheric and magnetospheric sources. The joint inversion of EM data for the daily and long-period bands led to a significantly improved model resolution in the upper mantle and MTZ. The conductivity profiles reveal significant lateral variability, which we interpreted in terms of upper mantle and MTZ water content by a stochastic coupling of electrical conductivity with constrains on the mantle thermo-chemical structure derived from the analysis of seismic data. Our results suggest the existence of a relatively dry MTZ beneath Europe and a water-enriched MTZ underneath North America and northern Asia.

Plain Language Summary

The amount of water (hydrogen) trapped in the Earth's interior has a strong influence on the evolution and dynamics of the planet, which ultimately controls the occurrence of earthquakes and volcanic eruptions. However, the distribution of water inside the Earth is yet not well-understood. Deep electromagnetic induction techniques analyze spatial and temporal changes in the Earth's magnetic field to detect variations in electrical conductivity inside the planet. As electrical conductivity is a characteristic of a rock that varies with temperature and the amount of water in its interior, we here present a methodology that combines different deep electromagnetic induction techniques to estimate the amount of water in different regions of the Earth mantle. Our analysis suggests the existence of little amounts of water in the mantle underneath Europe, whereas larger amounts are expected beneath North America and northern Asia. These findings help revealing the complexity of the water circulation in the deep mantle and can potentially be used to benchmark predictions from studies that simulate mantle dynamics.

1 Introduction

Constraining the water (hydrogen) distribution in Earth's interior is important for understanding its evolution and dynamics since water has a profound effect on rheological properties and melting relationships [e.g., *Hirschmann*, 2006; *Karato*, 2011]. High-pressure mineral-physics studies have reported that mantle transition zone (MTZ) minerals can store large amounts of water (~1–3 wt%), whereas much smaller amounts (~0.1–0.2 wt%) can be stored in upper mantle minerals [e.g., *Hirschmann et al.*, 2005; *Bolfan-Casanova*, 2005]. Supporting evidence for a relatively dry (~0.02 wt%) upper mantle and a hydrous (~1 wt%) MTZ has been provided by the analysis of mantle

xenoliths [e.g., *Peslier et al.*, 2010; *Peslier and Bizimis*, 2015] and ringwoodite inclusions found in a natural diamond that truly originated in the MTZ [*Pearson et al.*, 2014], respectively. However, the present distribution of water in the Earth's interior and the mechanisms for water exchange between different mantle reservoirs remain uncertain [e.g., *Ohtani et al.*, 2004; *Hirschmann*, 2006; *Bolfan-Casanova et al.*, 2006].

As electrical conductivity is a transport property that is highly sensitive to mantle temperature and the presence of water and melt [e.g., *Karato*, 2011; *Katsura and Yoshino*, 2015; *Khan*, 2016], deep electromagnetic (EM) sounding techniques play a fundamental role in mapping the distribution of water in the mantle by imaging variations in electrical conductivity [e.g., *Koyama et al.*, 2006; *Kelbert et al.*, 2009; *Shimizu et al.*, 2010; *Semenov and Kuvshinov*, 2012; *Koyama et al.*, 2014; *Sun et al.*, 2015]. These techniques rely on the fact that primary magnetic fields (e.g., those that originate in the magnetosphere) penetrate into the deep Earth and induce secondary signals by virtue of EM induction. EM variations in the daily band (4–24 hours) are mainly dominated by the ionospheric current system, while variations with periods longer than one day are generated by magnetospheric currents [e.g., *Finlay et al.*, 2017]. As penetration depth depends on frequency, analyzing these signals in as wide a range of periods as possible allows us to sense electrical conductivity variations in the widest depth range possible [e.g., *Püthe et al.*, 2015a]. However, EM sounding studies often rely on single-source data analysis facing the problem of limited depth resolution due to a limited frequency range imposed by various source morphologies [cf., *Kuvshinov*, 2008].

Only a few studies have attempted to combine EM responses from different sources. For instance, *Egbert and Booker* [1992] and *Bahr et al.* [1993] combined signals from magnetospheric and ionospheric origin recorded at geomagnetic observatories to obtain regional conductivity models of the mantle underneath North America and Europe, respectively. These studies, however, invoked simplistic source assumptions, which is likely to increase the chance of introducing source related model biases. Alternatively, *Olsen* [1998] accounted for a more complex source geometry (in the period range 3–720 hr) by incorporating estimates of horizontal gradients of the horizontal magnetic field. Given that direct measurement of these gradients on a single site is challenging in practice, the author estimated gradients from horizontal magnetic field components measured at an array of nearby observatories, which is limited to regions with a dense network of geomagnetic observatories (e.g., Europe). More recently, *Grayver et al.* [2017] jointly inverted the magnetospheric global response and ocean tidal signals from satellite magnetic field measurements, yielding a consistent global conductivity model of the oceanic upper mantle and transition zone.

Here, we perform inversions of daily (6–24 hours) and long-period (3–85 days) local responses recorded at a series of geomagnetic observatories to infer lateral variations in upper mantle and MTZ conductivity structure and water content. To isolate the influence of water on electrical conductivity from thermal effects, we follow *Khan* [2016] and combine phase equilibrium calculations, laboratory-

measured electrical conductivity of mantle minerals, and estimates of mantle temperature and major element chemistry derived from the analysis of short- and long-period seismic data using the results of *Munch et al.* [2020].

2 Methods

2.1 Multi-source EM global-to-local transfer functions

Signals due to the magnetospheric currents dominate natural geomagnetic variations at periods longer than one day [cf., *Finlay et al.*, 2017; *Olsen and Stolle*, 2017]. The source of these signals is often described via a single – first zonal – spherical harmonic, leading to the widely-used local C-response [*Banks*, 1969]. This transfer function (TF) relates vertical and horizontal components of the magnetic variations at an observational site. However, it is known that the magnetospheric source has a more complex structure, especially during the main phase of geomagnetic storms [e.g., *Daglis and Kozyra*, 2002; *Olsen and Kuvshinov*, 2004; *Balasis and Egbert*, 2006], thus potentially introducing errors in the estimated responses, resulting in biases in the retrieved conductivity structure [e.g., *Püthe et al.*, 2015b]. Furthermore, geomagnetic field variations in the period range between a few hours and one day are dominated by the ionospheric current systems which are characterized by a more complex morphology [e.g., *Yamazaki and Maute*, 2017]. This complexity invalidates simplistic source models that would allow the use of a TF similar to the C-response. To account for complex ionospheric and magnetospheric sources, we resort here to an alternative set of global-to-local transfer functions, $T_n^m(\mathbf{r}_a, \omega)$, that relate the vertical component of the magnetic field $Z(\mathbf{r}_a, \omega)$ at an observation site $\mathbf{r}_a = (a, \theta, \varphi)$ to a set of global spherical harmonic expansion (SHE) coefficients, $\varepsilon_n^m(\omega)$, that describe the source structure [*Püthe et al.*, 2015b]

$$Z(\mathbf{r}_a, \omega) = \sum_{n=1}^{N_\varepsilon} \sum_{m=-n}^{n} \varepsilon_n^m(\omega)\, T_n^m(\mathbf{r}_a, \omega), \tag{1}$$

where N_ε is the maximum (cut-off) degree for the external SHE coefficients, ω is the angular frequency, a denotes the Earth's mean radius, θ is the colatitude, and φ is the longitude.

The estimation of global-to-local TFs is a two step procedure: (i) external SHE coefficients describing the source are determined from horizontal components of the magnetic field measured at a global network of geomagnetic observatories assuming an a priori three-dimensional (3-D) Earth model, which consists of a mantle with a one-dimensional (1-D) conductivity distribution overlaid by a laterally-varying surface conductance layer; the latter approximates the nonuniform distribution of oceans and continents (see Appendix A for details on estimating "magnetospheric" source coefficients); and (ii) TFs are estimated by relating the vertical component of the magnetic field measured at every site of interest with the source coefficients determined in the previous step. The data for estimating "magnetospheric" TFs consist of hourly mean values of geomagnetic field variations measured at 132 mid-latitude (geomagnetic latitudes between ±6° and ±56°) permanent

geomagnetic observatories (see Figure S1) for the years 1998–2018 retrieved from the British Geological Survey (BGS) database [*Macmillan and Olsen*, 2013]. After removal of the main field and its secular variations using the CHAOS model [*Olsen et al.*, 2006], source coefficients and global-to-local transfer functions for the long-period band (3–85 days) were determined following the procedures described in *Püthe et al.* [2015b], which includes section-averaging [e.g., *Olsen*, 1998] and Huber-weighted robust least-squares methods [e.g., *Aster et al.*, 2005]. As for global-to-local TFs in the daily band (24, 12, 8, and 6 hours), we used those estimated by *Guzavina et al.* [2019] from the BGS database. Geographic and geomagnetic coordinate systems were used for estimating "daily" and "long-period" TFs, respectively.

2.2 Probabilistic inversion

We employed the probabilistic approach of *Tarantola and Valette* [1982] and the Metropolis algorithm [e.g., *Metropolis et al.*, 1953; *Hastings*, 1970] to determine the conductivity structure underneath each station from the estimated global-to-local TFs. Building on previous experience [*Munch et al.*, 2018], we reduced the burn-in stage of the Metropolis algorithm by using a global optimization technique [Covariance Matrix Adaptation Evolution Strategy; *Hansen and Ostermeier*, 2001] to obtain a good initial model $\mathbf{m_0}$ for every inversion. The solution of the non-linear inverse problem is then given in terms of the posterior probability distribution

$$\gamma(\mathbf{m}|\mathbf{d}) \propto \exp\left[-\frac{\phi(\mathbf{m},\mathbf{d})}{2}\right] \exp\left[-\frac{\beta}{p_m}\sum_{i=1}^{M}|\nabla \mathrm{m}_i|^{p_m}\right], \tag{2}$$

where $\mathbf{d}$ denotes observed data and $\mathbf{m} = [\lambda(\sigma_1)\cdots\lambda(\sigma_N)]$ represents the unknown conductivity structure, with $\lambda(\cdot)$ being a log-based transformation ensuring positivity of the argument. The subsurface was parametrized in terms of 25 layers ranging in thickness from 50 km in the upper mantle and MTZ to 400 km at the core-mantle boundary with a fixed core conductivity ($\sigma = 10^5$ S/m). The regularization parameter β was determined by means of an L-curve analysis [*Hansen*, 1999] performed on the models $\mathbf{m_0}$ and the scalar p_m was set to 1.5 which provides a good balance between sharp conductivity contrasts and smooth models [*Grayver and Kuvshinov*, 2016]. The data misfit term is given by

$$\phi(\mathbf{m},\mathbf{d}) = \sum_{k\in\mathcal{M}}\left(\frac{1}{N_k}\sum_{i=1}^{N_k}\left|w_i^k\,(f_i^k(\mathbf{m}) - d_i^k)\right|^2\right), \tag{3}$$

where $\mathcal{M}$ denote the EM methods in the daily and long-period bands and w^k, $f^k(\mathbf{m})$, and d^k are corresponding data weights (reciprocal of uncertainties), forward operator, and observed data, respectively. As discussed by *Grayver et al.* [2017], normalizing with the number of actual measurements (N_k) is an important aspect that helps balance the contribution of each EM technique.

2.3 Inference of water content from retrieved conductivity profiles

We interpreted the obtained conductivity profiles in terms of upper mantle and transition zone water content by comparing the retrieved models with laboratory-based conductivity profiles computed using the approach of *Khan* [2016]. To isolate the influence of water on electrical conductivity from thermal effects, we constrained mantle temperature and major element chemistry underneath each geomagnetic observatory by incorporating into the inversion probability density functions independently derived from the inversion of short- (P-to-s receiver functions) and long-period (Rayleigh wave phase velocities) seismic data from a nearby seismic station [*Munch et al.*, 2020, manuscript under review]. Mantle composition was parameterized in terms of a single variable that represents the amount of basalt in a basalt-harzburgite mixture, with the composition of basalt and harzburgite end-members described using the CFMASNa chemical model system comprising the oxides CaO-MgO-FeO-Al_2O_3-SiO_2-Na_2O. Mantle temperature was described in terms of an adiabat defined by the mantle potential temperature T_p, which represents the temperature that the mantle would have at the surface, if it ascended along an adiabat without undergoing melting [*McKenzie and Bickle*, 1988].

The laboratory-based conductivity profiles were computed from mineral phase equilibrium calculations and experimental measurements of mantle mineral conductivities. We employed the Gibbs free-energy minimization strategy of *Connolly* [2009] and the self-consistent thermodynamic formulation of *Stixrude and Lithgow-Bertelloni* [2005] with parameters given by *Stixrude and Lithgow-Bertelloni* [2011] to predict stable mineralogy (mineral modes) as a function of pressure, temperature, and composition. Several independent measurements of the electrical conductivity for major upper mantle and MTZ minerals exist. To minimize subjectivity, we here considered two databases built on the measurements of (i) Yoshino, Katsura, and coworkers (referred to as YK) and (ii) Karato, Dai, and coworkers (referred to as KD). Table 1 provides the list of data sources used to build the YK and KD databases. The laboratory-measured databases account for the effect of water content on the following hydrous minerals: olivine, orthopyroxene, clinopyroxene, wadsleyite, ringwoodite, and garnet (only KD database). Building on previous experience [e.g., *Khan*, 2016], we parameterized the water content of the mantle in terms of the water contents in olivine (upper mantle) and wadsleyite (transition zone). Water contents in orthopyroxene, clinopyroxene, and ringwoodite were estimated using the water partition coefficients based on measurements from *Inoue et al.* [2010] and *Ferot and Bolfan-Casanova* [2012]. Water content in garnet (only relevant for KD database) was estimated using the water partition coefficients derived by *Mookherjee and Karato* [2010].

Mineral	YK database	KD database
Olivine	*Yoshino and Katsura* [2009]	*Wang et al.* [2006]
	Yoshino et al. [2012]	*Karato* [2011]
Orthopyroxene	*Zhang et al.* [2012]	*Dai and Karato* [2009]
Clinopyroxene	*Zhao and Yoshino* [2016]	*Xu et al.* [2000]
Akimotoite	*Katsura et al.* [2007]	*Xu et al.* [2000]
Garnet	*Yoshino et al.* [2008a]	*Karato* [2011]
Wadsleyite	*Yoshino and Katsura* [2012]	*Dai and Karato* [2009]
Ringwoodite	*Yoshino et al.* [2008b]	*Huang et al.* [2005]
	Yoshino et al. [2012]	
	Yoshino and Katsura [2009]	
Ferropericlase	*Yoshino et al.* [2011]	*Xu et al.* [2000]
Bridgmanite	*Yoshino et al.* [2016]	*Xu et al.* [2000]
Ca-perovskite	*Xu et al.* [2000]	*Xu et al.* [2000]

Table 1. List of studies by Yoshino, Katsura, and coworkers (YK database) and Karato, Dai, and coworkers (KD database) from which the laboratory-based conductivity databases were compiled.

3 Results

3.1 Long-period transfer functions

As discussed above, we estimated global-to-local transfer functions in the period range 3–85 days from 20 years (1998–2018) of ground-based geomantic observatory data. In order to better account for the complexity of the source, magnetospheric time series were parameterized in terms of 13 SHE coefficients (ε_1^0,ε_1^1,ε_1^{-1},ε_2^0, ε_2^1,ε_2^{-1},ε_2^2,ε_2^{-2},ε_3^2,ε_3^{-2},ε_4^0,ε_4^1, and ε_4^{-1}). The choice of source coefficients aims at maximizing the coefficient of determination (i.e., measure of how well a proposed source geometry predicts the observed time series; see Figure S2), while minimizing the number of source terms that limits the maximum period for which multi-variate transfer functions can be estimated [*Püthe and Kuvshinov*, 2014] and that may result in over-fitting. All source terms were used to estimate long-period global-to-local transfer functions T_n^m, but only the dominant source term T_1^0 was considered in the inversion to retrieve the conductivity structure underneath each station because this TF is most sensitive to the radial structure of the Earth [*Kuvshinov*, 2008]. In the daily band, we also considered only TFs corresponding to dominant source terms, namely, T_p^{p+1} at periods $24/p$ hr ($p = 1 - 4$). As discussed in Section 2.1, the estimation of source coefficients requires the assumption of a mantle 1-D conductivity profile to separate the external (inducing) from the internal (induced) contributions in the measured geomagnetic variations. We find that differences

in the long-period TFs introduced by the choice of the mantle conductivity profile are within data uncertainties (see Figure S3).

Figure 1a depicts estimated long-period responses T_1^0, uncertainties, and squared coherencies (coh^2) for four geomagnetic observatories: Boulder (BOU, USA), Fürstenfeldbruck (FUR, Germany), Belsk (BEL, Poland), and Irkutsk (IRT, Russia). For comparison, transfer functions $\hat{T}_1^0$ estimated assuming that the source is described by the first zonal spherical harmonic are also shown. In this case, the TFs were derived from the local C-response $C(\mathbf{r}_a, \omega)$ – estimated using the Z/H method of *Banks* [1969] – as $\hat{T}_1^0(\mathbf{r}_a, \omega) = \frac{3\,C(\mathbf{r}_a,\omega)}{C(\mathbf{r}_a,\omega)+a} \cos\theta$. In agreement with previous studies [*Püthe et al.*, 2015b], we find that the incorporation of additional source terms increases the squared-coherency, especially at periods <10 days and geomagnetic latitudes >40°, thus decreasing the potential bias of the responses that could result from correlated noise and spatial aliasing [*Olsen*, 1998]. Figure 1b shows the average relative difference between T_1^0 and $\hat{T}_1^0$ as a function of geomagnetic colatitude. We observe that the use of simplistic source models results in significant differences of the estimated TFs, particularly for the imaginary part, which can potentially bias the inversion.

3.2 Data fit and recovered conductivity models

The transfer functions were individually inverted to determine the most probable set of conductivity profiles underneath 20 inland geomagnetic observatories (see Figure S4), for which synthetic TFs can be computed with low computational cost using analytical solutions for radial 1-D Earth models. Coastal and island geomagnetic observatories have been excluded from this analysis because calculation of synthetic TFs for these locations require the use of 3-D solvers to account for ocean induction effects [e.g., *Kuvshinov et al.*, 2002], making the use of Markov chain Monte Carlo methods [e.g., *Mosegaard and Tarantola*, 1995] impracticable.

We succeed at explaining the observed daily and long-period EM variations for 13 geomagnetic observatories (see Figures S6–S8), indicated in Figure S4 by red stars surrounded by black circles. However, we find a cluster of 7 stations located in Europe (black circles in Figure S4) for which the fit of daily transfer functions is unsatisfactory under the 1-D assumption (see Figures S6–S8). One can speculate that this reflects: 1) the presence of anomalously shallow 3-D structure underneath central Europe and the Mediterranean linked to the subduction and ponding of slabs in the MTZ as suggested by seismic tomography [e.g., *Zhu et al.*, 2015; *Cottaar and Deuss*, 2016]; or 2) artifacts due to the presence of noise (e.g., signals due to polar eletrojet currents) that are not accounted for in the presently used source parameterization.

Figure S5 illustrates the posterior probability distributions obtained when inverting daily and long-period signals separately and jointly at a single station (Alice Spring in Australia). In agreement with previous studies [e.g., *Munch et al.*, 2018], long-period signals best constrain the conductivity

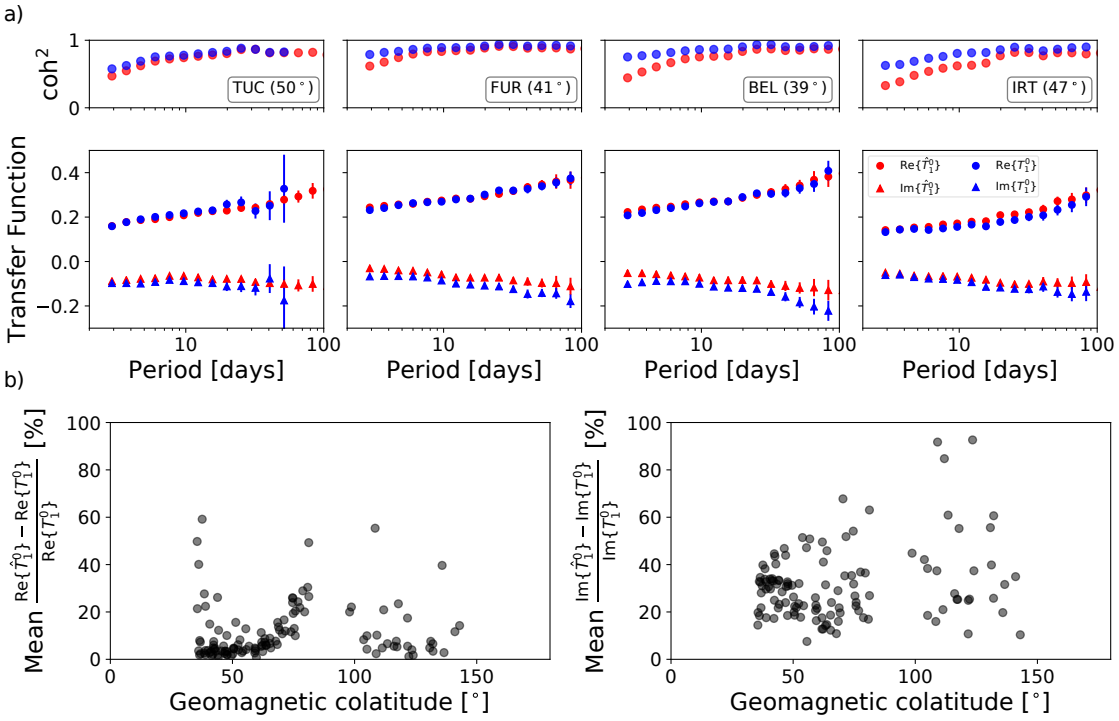

Figure 1. Example of experimental global-to-local transfer functions. a) Real (positive) and imaginary (negative) parts of the experimental global-to-local (blue) transfer functions T_1^0 (bottom row) and squared coherencies coh^2 (top row) estimated in this study for Boulder (BOU), Fürstenfeldbruck (FUR), Belsk (BEL), and Irkutsk (IRT) geomagnetic observatories. Error bars indicate uncertainties of the experimental transfer functions. For comparison, transfer functions $\hat{T}_1^0$ obtained for a case when the source is described by the first zonal spherical harmonic are shown in red. b) Mean relative differences between the real (left) and imaginary (right) parts of T_1^0 and $\hat{T}_1^0$ as a function of geomagnetic colatitude.

structure in the depth range between 400 and 1400 km (see Figure S5b), while daily variations provide information on the conductivity structure between 200 and 500 km depth (see Figure S5a) [e.g., *Koch and Kuvshinov*, 2013]. The models obtained from the joint inversion of daily and long-period signals (see Figure S5c) manage to resolve the conductivity structure in the upper mantle (200–400 km depth), MTZ (400–660 km depth), and the uppermost lower mantle (660–1400 km depth).

3.3 Constraints on upper mantle and transition zone water content

We determined the range of water contents in olivine and wadsleyite that best explain the inverted conductivity profiles between 200 and 1200 km depth. This was achieved by comparing the inverted conductivity models with laboratory-based conductivity profiles (described in Section 2.3) using an L_2–norm misfit function and the Metropolis algorithm. In particular, we focus on 8 geomagnetic observatories for which probability density functions of the mantle potential temperature and composition (basalt fraction) derived from the inversion of short- and long-period seismic data [*Munch et al.*, 2020] recorded at a nearby station (indicated by triangles in Figure S4) are available.

Figure 2 summarizes the conductivity models obtained from the joint inversion of long-period and daily signals (black) and best-fitting laboratory-based conductivity profiles (green). Laboratory-based conductivity profiles implicitly incorporate discontinuities across the major phase transitions (olivine → wadsleyite, wadsleyite → ringwoodite, and ringwoodite → bridgmanite+ferropericlase), whereas the conductivity models retrieved from the inversion of observed EM responses are smoother down to depths of ~1000 km. We find an overall agreement between the inverted conductivity models and laboratory-based conductivity profiles particularly in the upper mantle and MTZ. However, we observe that laboratory-based conductivity profiles are systematically more conductive in the lower mantle (800–1200 km depth) than the conductivity models derived from the observed data. This difference might reflect that 1) temperature estimates derived from the inversion of seismic data might be biased towards higher temperatures; or 2) the laboratory-based conductivity databases considered in this work tend to overestimate the electrical conductivity of lower mantle minerals. Future work should aim at refining the laboratory-based mineral conductivity databases, particularly for lower-mantle minerals, as the degree to which hydrogen affects the electrical conductivity of lower mantle minerals remains uncertain. In this light, determining the influence of hydrogen on electrical conductivity in the lower mantle minerals is critical to improve the current understanding of the water distribution in the deep mantle and the circulation between the various reservoirs.

Figure 3 depicts inferences on water content in the upper mantle and MTZ minerals olivine (C_w^{ol}) and wadsleyite (C_w^{wad}) obtained using the YK and KD databases. The former database generally leads to a significantly more hydrated upper mantle and MTZ. As discussed by *Khan and Shankland* [2012], this difference arises from the fact that the KD database tends to result in higher electrical conductivities for a given water content. The use of the YK database results in anomalously high

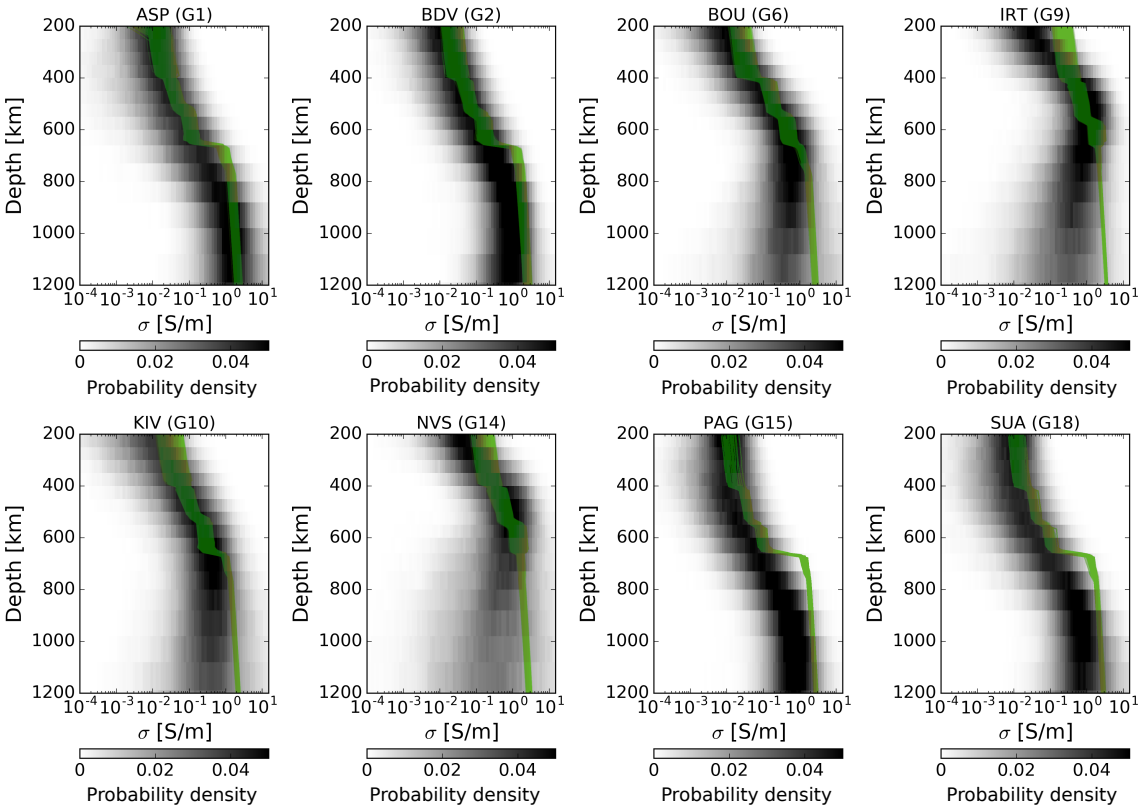

Figure 2. Posterior probability distributions of electrical conductivity (σ) retrieved from the joint inversion of daily and long-period transfer functions (black) and best-fitting laboratory-based conductivity profiles (green) for the KD database. The geographic location of each geomagnetic observatory is shown in Figure S4 and station acronyms are defined in Table S1. Best-fitting laboraty-based conductivity profiles obtained using the YK database are shown in Figure S9.

water contents (C_w^{ol}~0.3 wt% and C_w^{wad}~1.9 wt%) underneath stations located in northern Asia (NVS and IRT). These estimates significantly exceed the experimentally-determined water storage capacity of mantle minerals [e.g., *Hirschmann et al.*, 2005; *Litasov et al.*, 2011], which would result in the accumulation of partial melt atop the MTZ [*Bercovici and Karato*, 2003]. However, no evidence for the existence of a melt layer (i.e., negative amplitudes on the receiver function waveforms due to a low shear-wave velocity anomaly) is observed in the seismic data and further analysis focuses on estimates derived with the KD database.

In agreement with previous studies [e.g., *Karato*, 2011; *Fullea et al.*, 2011; *Jones et al.*, 2012; *Khan and Shankland*, 2012], our results indicate a relatively dry upper mantle (C_w^{ol}<0.02 wt%) underneath all stations, whereas significat lateral variability in MTZ water content is observed. We find relatively low MTZ water contents (C_w^{wad} <0.05 wt%) in Australia (ASP) and Europe (BDV,

PAG, SUA, and KIV), whereas moderate (C_w^{wad}~0.15 wt%) and high water contents (C_w^{wad}~0.3 wt%) are required to explain the inverted conductivity profiles in Asia (IRT and NVS) and North America (BOU), respectively. A dry MTZ below Europe has already been suggested by *Utada et al.* [2009] from the joint analysis of seismic and electromagnetic models. In agreement with MTZ water contents experimentally determined by *Freitas et al.* [2017], our estimates suggest that the near-water saturated conditions implied by hydrous ringwoodite inclusions found in a natural diamond [*Pearson et al.*, 2014] are not representative of the whole MTZ.

4 Conclusions

In this study, we combined EM responses in a wide period band to infer the electrical conductivity structure underneath a set of inland geomagnetic observatories, while accounting for complex spatial structure of the magnetospheric and ionospheric sources [*Püthe et al.*, 2015b]. We found that simplistic source models are likely to introduce significant errors in the estimated transfer functions and therefore, bias the inferred conductivity models. Furthermore, the incorporation of daily-band responses (6–24 h) into the inversion leads to improved model resolution, especially in the upper mantle and transition zone.

The retrieved conductivity models were subsequently interpreted in terms of variations in upper mantle (olivine) and transition zone (wadsleyite) water content by combining mineral phase equilibria calculations, laboratory-based electrical conductivity measurements, and estimates on mantle temperature and major element chemistry derived independently from the inversion of short- and long-period seismic data. We find the existence of a relatively dry transition zone beneath Europe (C_w^{wad} <0.05 wt%) and a water-enriched (C_w^{wad}~0.3 wt%) transition zone underneath North America and northern Asia. These findings suggest that the near-water saturated conditions hinted at by hydrous ringwoodite inclusions found in a natural diamond [*Pearson et al.*, 2014] are not likely to be representative of the entire MTZ.

The methodology presented here provides quantitative constraints on water content in the upper mantle and transition zone. To move beyond the current results and improve our understanding of the water distribution in the deep mantle and mantle water circulation, future work should aim at: 1) extending the geographical distribution of geomagnetic observatories to include data from coastal and island; and 2) inverting EM and seismic data jointly by means of an integrated approach [e.g., *Khan*, 2016]. The former demands the use of 3-D EM solvers to account for the ocean induction effect [e.g., *Kuvshinov et al.*, 2002], which makes the implementation of Markov chain Monte Carlo methods impracticable. The latter requires a refinement of the laboratory-based electrical conductivity databases to lower-mantle minerals, and the extension of the thermodynamic database employed for mineral phase equilibria calculations to account for effects related to oxygen fugacity, water content, and melt.

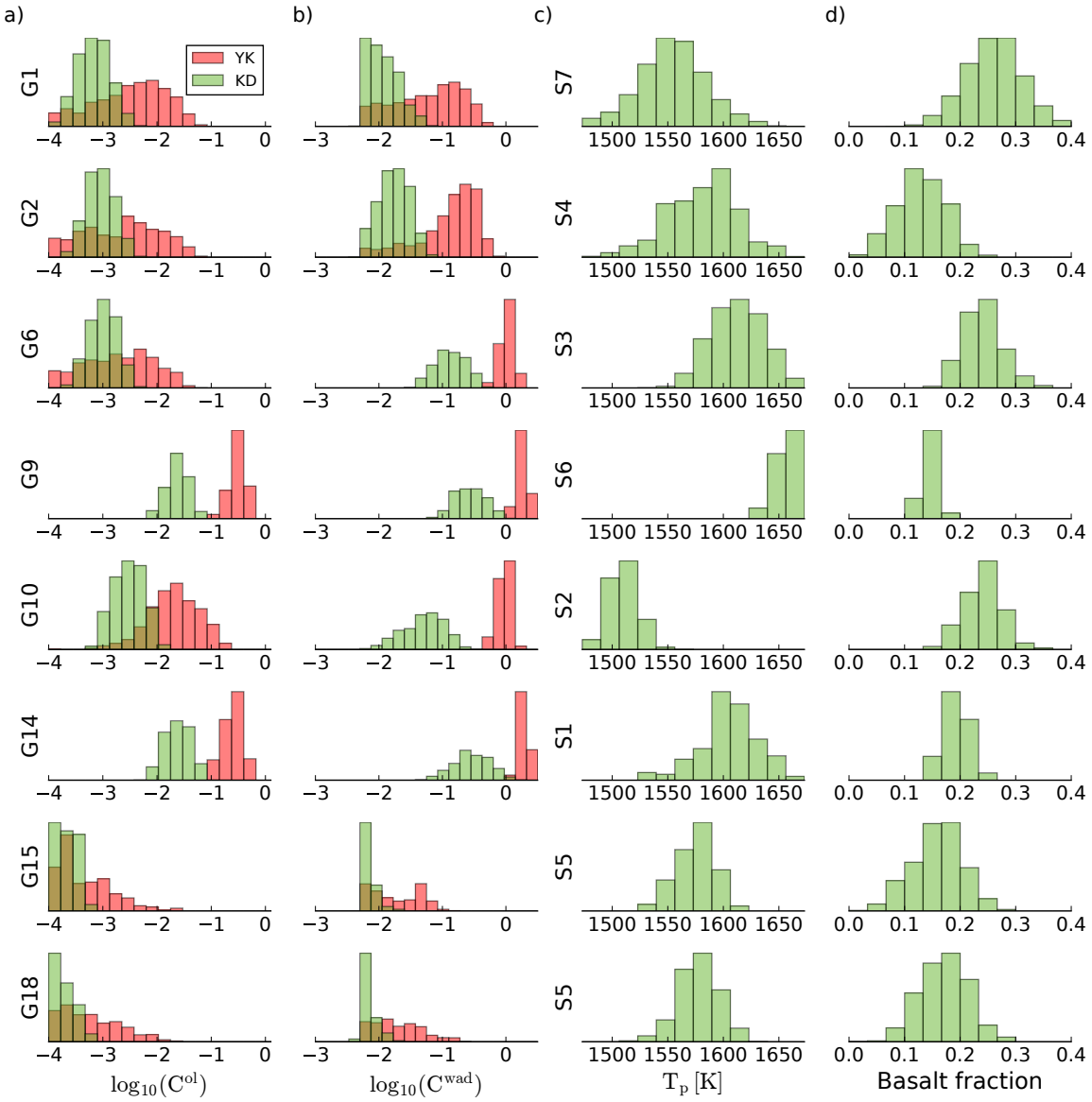

Figure 3. Sampled water content in (a) olivine and (b) wadsleyite retrieved using the Yoshino-Katsura (YK) and Karato-Dai (KD) electrical conductivity databases. Water contents are given in terms of $C^x = C^x_w/C^x_w$, where x denotes either of the minerals olivine and wadsleyite, C^x_w is in wt%, and $C^0_w = 1$ wt%. Constraints on the probability distribution of (c) mantle potential temperature (T_p) and (d) composition (basalt fraction) were obtained from the inversion of P–to–s receiver functions and Rayleigh wave phase velocities [*Munch et al.*, 2020]. Station codes are defined in Table S1.

Acknowledgments

F.D.M. was supported by a grant from the Swiss National Science Foundation (Project No. 159907). A.G. and A.V.K. were supported by ESA through the Swarm DISC project. M.G. was supported by

ETH Grant No. ETH-3215-2. Moreover, the authors would like to acknowledge the British Geological Survey (BGS), WDC Geomagnetism (Edinburgh), INTERMAGNET and the many Institutes around the World that operate magnetic observatories. Time series of geomagnetic field components used in this study are available on `ftp://ftp.nerc-murchison.ac.uk/geomag/Swarm/AUX_OBS/hour`.

Appendix A: Estimation of magnetospheric source coefficients

Maxwell's equations describe the spatio-temporal behavior of electromagnetic fields and can be formulated in frequency domain as

$$\frac{1}{\mu_0}\nabla \times \mathbf{B}(\mathbf{r},\omega) = \sigma(\mathbf{r})\mathbf{E}(\mathbf{r},\omega) + \mathbf{j}^{\text{ext}}(\mathbf{r},\omega), \tag{4}$$

$$\nabla \times \mathbf{E}(\mathbf{r},\omega) = i\omega\mathbf{B}(\mathbf{r},\omega), \tag{5}$$

where $\mathbf{B}$ and $\mathbf{E}$ represent the complex Fourier transforms of magnetic flux density and electric field at a location $\mathbf{r} = (r, \vartheta, \varphi)$. The distance from the Earth's center is denoted by r, ϑ is the colatitude, and φ is the longitude. Furthermore, $\mathbf{j}^{\text{ext}}(\mathbf{r},\omega)$ is the complex Fourier transform of an impressed source current density, $\sigma(\mathbf{r})$ represents the electrical conductivity distribution in the media, ω is the angular frequency, and μ_0 is the magnetic permeability of free space. Given that deep electromagnetic (EM) studies consider induction due to natural current systems which vary on time scales between a few hours and a few months, displacement currents are here neglected.

Above the conducting Earth and below the region enclosed by the current $\mathbf{j}^{\text{ext}}$, Eq. (4) reduces to $\nabla \times \mathbf{B} = 0$, thus $\mathbf{B}$ is a potential field that can described as a gradient of a scalar potential V

$$\mathbf{B} = -\nabla V. \tag{6}$$

Since $\nabla \cdot \mathbf{B} = 0$, then V satisfies Laplace's equation ($\nabla^2 V = 0$) and hence, can be decomposed into external and internal parts such that $V = V^{\text{ext}} + V^{\text{int}}$, where

$$V^{\text{ext}} = a \sum_{n=1}^{N_\varepsilon} \sum_{m=-n}^{n} \varepsilon_n^m(\omega) \left(\frac{r}{a}\right)^n Y_n^m(\vartheta,\varphi), \tag{7}$$

$$V^{\text{int}} = a \sum_{k=1}^{N_\iota} \sum_{l=-k}^{k} \iota_k^l(\omega) \left(\frac{r}{a}\right)^{-(k+1)} Y_k^l(\vartheta,\varphi), \tag{8}$$

where $\varepsilon_n^m(\omega)$ and $\iota_k^l(\omega)$ are the spherical harmonic expansion (SHE) coefficients of the external (inducing) and internal (induced) parts of the potential, N_ε and N_ι are the maximum (cut-off) degrees for external and internal coefficients, respectively, and Y_n^m is the spherical harmonic of degree n and order m

$$Y_n^m(\vartheta,\varphi) = P_n^{|m|}(\cos\vartheta)e^{im\varphi}, \tag{9}$$

where $P_n^{|m|}(\cos\vartheta)$ corresponds to the Schmidt quasi-normalized associated Legendre function of degree n and order $|m|$. Note that in Eqs (7) and (8), we use different indices for external and internal coefficients to account for the 3-D conductivity distribution. In a 1-D Earth (in which conductivity is only a function of depth), every external coefficient only induces one internal coefficient of the same degree and order. They are linearly related by the (scalar) Q-response, which is defined as

$$\iota_n^m(\omega) = Q_n(\omega)\varepsilon_n^m(\omega). \tag{10}$$

Note that in 1-D case Q_n is independent of the order m [e.g., **?**] and $N_\varepsilon = N_\iota$. In a 3-D Earth, however, every external coefficient ε_n^m induces a whole series of internal coefficients ι_k^l such that we can write

$$\iota_k^l(\omega) = \sum_{n=1}^{N_\varepsilon}\sum_{m=-n}^{n} Q_{kn}^{lm}(\omega)\varepsilon_n^m(\omega), \tag{11}$$

where the Q_{kn}^{lm} form a 2-D array of transfer functions we refer to as Q-matrix. The diagonal elements of this matrix mostly describe the bulk conductivity and in case of a layered (1-D) Earth they are equivalent to the scalar Q-responses. The off-diagonal elements describe a transfer of energy to coefficients of different degree and order, which only occurs if the subsurface has a 3-D structure. Note that our a priori 3-D Earth's model consists of a mantle with 1-D conductivity distribution overlaid by a surface layer of known laterally-variable conductance; the latter approximates nonuniform distribution of oceans and continents. Our numerical experiments shows that the diagonal elements of corresponding Q-matrix are dominant for the considered period range (3–85 days). Therefore, exploiting Eqs. (6)-(8) and (11), the magnetic field on the surface of the Earth, $\mathbf{r}_a = (a, \vartheta, \varphi)$, can be written as

$$B_r(\mathbf{r}_a, \omega) = -\sum_{n=1}^{N_\varepsilon}\sum_{m=-n}^{n} \varepsilon_n^m(\omega)\big[n - (n+1)Q_{nn}^{mm}(\omega)\big]Y_n^m(\vartheta, \varphi), \tag{12}$$

$$\mathbf{B}_\tau(\mathbf{r}_a, \omega) = -\sum_{n=1}^{N_\varepsilon}\sum_{m=-n}^{n} \varepsilon_n^m(\omega)\big[1 + Q_{nn}^{mm}(\omega)\big]\nabla_\perp Y_n^m(\vartheta, \varphi), \tag{13}$$

where subscript τ denotes the tangential part of $\mathbf{B}$ and $\nabla_\perp$ is the surface gradient. With the following denotation

$$v_n^m(\omega) = \varepsilon_n^m(\omega)\big[1 + Q_{nn}^{mm}(\omega)\big], \tag{14}$$

time domain equivalent of Eq. (13) reads

$$\mathbf{B}_\tau(\mathbf{r}_a, t) = -\sum_{n=1}^{N_\varepsilon}\sum_{m=-n}^{n} v_n^m(t)\nabla_\perp Y_n^m(\vartheta, \varphi). \tag{15}$$

In this study, we estimated external source coefficients $\epsilon_n^m(t)$ following the procedure proposed by *Püthe et al.* [2015b]. This procedure can be summarized as follows:

(1) Collection of hourly-mean time series of geomagnetic field components from mid-latitude permanent observatories (see Figure S1) from the British Geological Survey database [*Macmillan and Olsen*, 2013].

(2) Removal of the main field and its secular variations using the CHAOS model [*Olsen et al.*, 2006].

(3) Detrend each magnetic field component using cubic B-splines.

(4) Rotation of the horizontal magnetic field components from geographic to geomagnetic coordinates using geomagnetic north pole coordinates for the year 2010.

(5) Estimation of v_n^m for each time instant t from the tangential components of the observed magnetic field in geomagnetic coordinates using Eq. (15) and a Huber-weighted robust least-squares method [e.g., *Aster et al.*, 2005]. Weights are meant to counteract potential biases introduced by cluster of stations (e.g., the high concentrations of observatories in the Northern hemisphere). At each time instant t, we triangulate the spatial distribution of observatories (via calculating the convex hull). Weights are then estimated as the surface area of the spherical triangle that has a given observatory as its center.

(6) Separation of internal and external contributions as follows:

A. Transformation of the unseparated coefficients $v_n^m(t)$ into frequency domain.

B. Computation of radial magnetic field $B_{n,r}^m(\mathbf{r}_a, \omega)$ induced by unit amplitude spherical harmonic sources ($\epsilon_n^m = 1$) in frequency domain using a numerical solver based on integral equation approach [*Kuvshinov*, 2008]. As mentioned above, computations are performed in a priori 3-D Earth's model consisting of a mantle with 1-D conductivity distribution overlaid by a surface layer of laterally-variable conductance.

C. Calculation of $Q_{nn}^{mm}(\omega)$ from the computed $B_{n,r}^m(\mathbf{r}_a, \omega)$ as [*Püthe and Kuvshinov*, 2014]

$$Q_{nn}^{mm}(\omega) = \frac{1}{(n+1)||Y_n^m||^2} \int_\Omega \left[B_{n,r}^m(\mathbf{r}_a, \omega) - B_{n,r}^{m,ext}(\mathbf{r}_a)\right) \hat{Y}_n^m(\vartheta, \varphi) ds. \tag{16}$$

Here $\hat{Y}_n^m$ denotes complex conjugation Y_n^m, Ω is the complete solid angle, $ds = \sin\vartheta d\vartheta d\varphi$, and $||Y_n^m||^2$ is the squared norm of the spherical harmonic Y_n^m, and $B_{n,r}^{m,ext}$ is the external part of radial magnetic field, i.e.

$$B_{n,r}^{m,ext}(\mathbf{r}_a) = -nY_n^m(\vartheta, \varphi). \tag{17}$$

Substituting Eq. (17) into Eq. (16) we have

$$Q_{nn}^{mm}(\omega) = \frac{1}{(n+1)||Y_n^m||^2} \int_\Omega B_{n,r}^m(\mathbf{r}_a, \omega) \hat{Y}_n^m(\vartheta, \varphi) ds + \frac{n}{n+1}. \tag{18}$$

D. Separation of internal and external contributions using Eq. (14)

$$\epsilon_n^m(\omega) = v_n^m(\omega)/[1 + Q_{nn}^{mm}(\omega)].$$

E. Transformation of the external coefficients $\epsilon_n^m(\omega)$ into time domain.

References

Aster, R., B. Borchers, and C. Thurber (2005), Parameter estimation and inverse problems: Elsevier academic.

Bahr, K., N. Olsen, and T. J. Shankland (1993), On the combination of the magnetotelluric and the geomagnetic depth sounding method for resolving an electrical conductivity increase at 400 km depth, *Geophysical research letters*, *20*(24), 2937–2940.

Balasis, G., and G. D. Egbert (2006), Empirical orthogonal function analysis of magnetic observatory data: Further evidence for non-axisymmetric magnetospheric sources for satellite induction studies, *Geophysical research letters*, *33*(11).

Banks, R. (1969), Geomagnetic variations and the electrical conductivity of the upper mantle, *Geophysical Journal International*, *17*(5), 457–487.

Bercovici, D., and S.-i. Karato (2003), Whole-mantle convection and the transition-zone water filter, *Nature*, *425*(6953), 39–44.

Bolfan-Casanova, N. (2005), Water in the Earth's mantle, *Mineralogical Magazine*, *69*(3), 229–257.

Bolfan-Casanova, N., C. A. Mccammon, and S. J. Mackwell (2006), Water in transition zone and lower mantle minerals, *GEOPHYSICAL MONOGRAPH-AMERICAN GEOPHYSICAL UNION*, *168*, 57.

Connolly, J. (2009), The geodynamic equation of state: what and how, *Geochemistry, Geophysics, Geosystems*, *10*(10).

Cottaar, S., and A. Deuss (2016), Large-scale mantle discontinuity topography beneath Europe: Signature of akimotoite in subducting slabs, *Journal of Geophysical Research: Solid Earth*, *121*(1), 279–292.

Daglis, I., and J. Kozyra (2002), Outstanding issues of ring current dynamics, *Journal of atmospheric and solar-terrestrial physics*, *64*(2), 253–264.

Dai, L., and S.-i. Karato (2009), Electrical conductivity of wadsleyite at high temperatures and high pressures, *Earth and Planetary Science Letters*, *287*(1), 277–283.

Egbert, G. D., and J. R. Booker (1992), Very long period magnetotellurics at Tucson observatory: implications for mantle conductivity, *Journal of Geophysical Research: Solid Earth*, *97*(B11), 15,099–15,112.

Ferot, A., and N. Bolfan-Casanova (2012), Water storage capacity in olivine and pyroxene to 14GPa: Implications for the water content of the Earth's upper mantle and nature of seismic discontinuities, *Earth and Planetary Science Letters*, *349*, 218–230.

Finlay, C., V. Lesur, E. Thébault, F. Vervelidou, A. Morschhauser, and R. Shore (2017), Challenges handling magnetospheric and ionospheric signals in internal geomagnetic field modelling.

Freitas, D., G. Manthilake, F. Schiavi, J. Chantel, N. Bolfan-Casanova, M. Bouhifd, and D. Andrault (2017), Experimental evidence supporting a global melt layer at the base of the Earth's upper

mantle, *Nature communications*, *8*(1), 2186.

Fullea, J., M. Muller, and A. Jones (2011), Electrical conductivity of continental lithospheric mantle from integrated geophysical and petrological modeling: Application to the Kaapvaal Craton and Rehoboth Terrane, southern Africa, *Journal of Geophysical Research: Solid Earth*, *116*(B10).

Grayver, A., F. Munch, A. Kuvshinov, A. Khan, T. Sabaka, and L. Tøffner-Clausen (2017), Joint inversion of satellite-detected tidal and magnetospheric signals constrains electrical conductivity and water content of the upper mantle and transition zone, *Geophysical Research Letters*.

Grayver, A. V., and A. V. Kuvshinov (2016), Exploring equivalence domain in nonlinear inverse problems using Covariance Matrix Adaption Evolution Strategy (CMAES) and random sampling, *Geophysical Journal International*, *205*(2), 971–987.

Guzavina, M., A. Grayver, and A. Kuvshinov (2019), Probing upper mantle electrical conductivity with daily magnetic variations using global-to-local transfer functions, *Geophysical Journal International*, *219*(3), 2125–2147.

Hansen, N., and A. Ostermeier (2001), Completely derandomized self-adaptation in evolution strategies, *Evolutionary computation*, *9*(2), 159–195.

Hansen, P. C. (1999), The L-curve and its use in the numerical treatment of inverse problems.

Hastings, W. K. (1970), Monte Carlo sampling methods using Markov chains and their applications, *Biometrika*, *57*(1), 97–109.

Hirschmann, M. M. (2006), Water, melting, and the deep Earth H2O cycle, *Annu. Rev. Earth Planet. Sci.*, *34*, 629–653.

Hirschmann, M. M., C. Aubaud, and A. C. Withers (2005), Storage capacity of H_2O in nominally anhydrous minerals in the upper mantle, *Earth and Planetary Science Letters*, *236*(1), 167–181.

Huang, X., Y. Xu, and S.-i. Karato (2005), Water content in the transition zone from electrical conductivity of wadsleyite and ringwoodite, *Nature*, *434*(7034), 746.

Inoue, T., T. Wada, R. Sasaki, and H. Yurimoto (2010), Water partitioning in the Earth's mantle, *Physics of the Earth and Planetary Interiors*, *183*(1), 245–251.

Jones, A. G., J. Fullea, R. L. Evans, and M. R. Muller (2012), Water in cratonic lithosphere: Calibrating laboratory-determined models of electrical conductivity of mantle minerals using geophysical and petrological observations, *Geochemistry, Geophysics, Geosystems*, *13*(6).

Karato, S.-i. (2011), Water distribution across the mantle transition zone and its implications for global material circulation, *Earth and Planetary Science Letters*, *301*(3), 413–423.

Katsura, T., and T. Yoshino (2015), Heterogeneity of electrical conductivity in the oceanic upper mantle, in *The Earth's Heterogeneous Mantle*, pp. 173–204, Springer.

Katsura, T., S. Yokoshi, K. Kawabe, A. Shatskiy, M. Okube, H. Fukui, E. Ito, A. Nozawa, and K.-i. Funakoshi (2007), Pressure dependence of electrical conductivity of (Mg, Fe) SiO3 ilmenite, *Physics and Chemistry of Minerals*, *34*(4), 249–255.

Kelbert, A., A. Schultz, and G. Egbert (2009), Global electromagnetic induction constraints on transition-zone water content variations, *Nature*, *460*(7258), 1003–1006.

Khan, A. (2016), On Earth's mantle constitution and structure from joint analysis of geophysical and laboratory-based data: An example, *Surveys in Geophysics*, *37*(1), 149–189.

Khan, A., and T. Shankland (2012), A geophysical perspective on mantle water content and melting: Inverting electromagnetic sounding data using laboratory-based electrical conductivity profiles, *Earth and Planetary Science Letters*, *317*, 27–43.

Koch, S., and A. Kuvshinov (2013), Global 3-D EM inversion of Sq variations based on simultaneous source and conductivity determination: concept validation and resolution studies, *Geophysical Journal International*, *195*(1), 98–116.

Koyama, T., H. Shimizu, H. Utada, M. Ichiki, E. Ohtani, and R. Hae (2006), Water content in the mantle transition zone beneath the north pacific derived from the electrical conductivity anomaly, *Earth's Deep Water Cycle*, pp. 171–179.

Koyama, T., A. Khan, and A. Kuvshinov (2014), Three-dimensional electrical conductivity structure beneath Australia from inversion of geomagnetic observatory data: evidence for lateral variations in transition-zone temperature, water content and melt, *Geophysical Journal International*, *196*(3), 1330.

Kuvshinov, A. (2008), 3-D global induction in the oceans and solid Earth: recent progress in modeling magnetic and electric fields from sources of magnetospheric, ionospheric and oceanic origin, *Surveys in geophysics*, *29*(2), 139–186.

Kuvshinov, A. V., N. Olsen, D. B. Avdeev, and O. V. Pankratov (2002), Electromagnetic induction in the oceans and the anomalous behaviour of coastal C-responses for periods up to 20 days, *Geophysical research letters*, *29*(12).

Litasov, K. D., A. Shatskiy, E. Ohtani, and T. Katsura (2011), Systematic study of hydrogen incorporation into Fe-free wadsleyite, *Physics and Chemistry of Minerals*, *38*(1), 75–84.

Macmillan, S., and N. Olsen (2013), Observatory data and the Swarm mission, *Earth, Planets and Space*, *65*(11), 1355–1362.

McKenzie, D., and M. Bickle (1988), The volume and composition of melt generated by extension of the lithosphere, *Journal of petrology*, *29*(3), 625–679.

Metropolis, N., A. W. Rosenbluth, M. N. Rosenbluth, A. H. Teller, and E. Teller (1953), Equation of state calculations by fast computing machines, *The journal of chemical physics*, *21*(6), 1087–1092.

Mookherjee, M., and S.-i. Karato (2010), Solubility of water in pyrope-rich garnet at high pressures and temperature, *Geophysical Research Letters*, *37*(3).

Mosegaard, K., and A. Tarantola (1995), Monte Carlo sampling of solutions to inverse problems, *Journal of Geophysical Research: Solid Earth*, *100*(B7), 12,431–12,447.

Munch, F., A. Grayver, A. Kuvshinov, and A. Khan (2018), Stochastic inversion of geomagnetic observatory data including rigorous treatment of the ocean induction effect with implications for transition zone water content and thermal structure, *Journal of Geophysical Research: Solid Earth*, *123*(1), 31–51.

Munch, F., A. Khan, B. Tauzin, M. van Driel, and D. Giardini (2020), Seismological evidence for the existence of thermo-chemical heterogeneity in Earth's continental mantle, *manuscript under consideration for publication in Earth and Planetary Science Letters*.

Ohtani, E., K. Litasov, T. Hosoya, T. Kubo, and T. Kondo (2004), Water transport into the deep mantle and formation of a hydrous transition zone, *Physics of the Earth and Planetary Interiors*, *143*, 255–269.

Olsen, N. (1998), The electrical conductivity of the mantle beneath Europe derived from C-responses from 3 to 720 hr, *Geophysical Journal International*, *133*(2), 298–308.

Olsen, N., and A. Kuvshinov (2004), Modeling the ocean effect of geomagnetic storms, *Earth, planets and space*, *56*(5), 525–530.

Olsen, N., and C. Stolle (2017), Magnetic signatures of ionospheric and magnetospheric current systems during geomagnetic quiet conditions—an overview, *Space Science Reviews*, *206*(1-4), 5–25.

Olsen, N., H. Lühr, T. J. Sabaka, M. Mandea, M. Rother, L. Tøffner-Clausen, and S. Choi (2006), CHAOS– A model of the Earth's magnetic field derived from CHAMP, ørsted, and SAC-C magnetic satellite data, *Geophysical Journal International*, *166*(1), 67–75.

Pearson, D., F. Brenker, F. Nestola, J. McNeill, L. Nasdala, M. Hutchison, S. Matveev, K. Mather, G. Silversmit, S. Schmitz, et al. (2014), Hydrous mantle transition zone indicated by ringwoodite included within diamond, *Nature*, *507*(7491), 221.

Peslier, A. H., and M. Bizimis (2015), Water in Hawaiian peridotite minerals: A case for a dry metasomatized oceanic mantle lithosphere, *Geochemistry, Geophysics, Geosystems*, *16*(4), 1211–1232.

Peslier, A. H., A. B. Woodland, D. R. Bell, and M. Lazarov (2010), Olivine water contents in the continental lithosphere and the longevity of cratons, *Nature*, *467*(7311), 78.

Püthe, C., and A. Kuvshinov (2014), Mapping 3-D mantle electrical conductivity from space: a new 3-D inversion scheme based on analysis of matrix Q-responses, *Geophysical Journal International*, *197*(2), 768–784.

Püthe, C., A. Kuvshinov, A. Khan, and N. Olsen (2015a), A new model of Earth's radial conductivity structure derived from over 10 yr of satellite and observatory magnetic data, *Geophysical Journal International*, *203*(3), 1864–1872.

Püthe, C., A. Kuvshinov, and N. Olsen (2015b), Handling complex source structures in global EM induction studies: from C-responses to new arrays of transfer functions, *Geophysical Journal*

International, *201*(1), 318–328.

Semenov, A., and A. Kuvshinov (2012), Global 3-D imaging of mantle conductivity based on inversion of observatory C-responses–II. Data analysis and results, *Geophysical Journal International*, *191*(3), 965–992.

Shimizu, H., H. Utada, K. Baba, T. Koyama, M. Obayashi, and Y. Fukao (2010), Three-dimensional imaging of electrical conductivity in the mantle transition zone beneath the North Pacific Ocean by a semi-global induction study, *Physics of the Earth and Planetary Interiors*, *183*(1), 252–269.

Stixrude, L., and C. Lithgow-Bertelloni (2005), Thermodynamics of mantle minerals-I. physical properties, *Geophysical Journal International*, *162*(2), 610–632.

Stixrude, L., and C. Lithgow-Bertelloni (2011), Thermodynamics of mantle minerals-II. Phase equilibria, *Geophysical Journal International*, *184*(3), 1180–1213.

Sun, J., A. Kelbert, and G. Egbert (2015), Ionospheric current source modeling and global geomagnetic induction using ground geomagnetic observatory data, *Journal of Geophysical Research: Solid Earth*, *120*(10), 6771–6796.

Tarantola, A., and B. Valette (1982), Generalized nonlinear inverse problems solved using the least squares criterion, *Reviews of Geophysics*, *20*(2), 219–232.

Utada, H., T. Koyama, M. Obayashi, and Y. Fukao (2009), A joint interpretation of electromagnetic and seismic tomography models suggests the mantle transition zone below Europe is dry, *Earth and Planetary Science Letters*, *281*(3), 249–257.

Wang, D., M. Mookherjee, Y. Xu, and S.-i. Karato (2006), The effect of water on the electrical conductivity of olivine, *Nature*, *443*(7114), 977.

Xu, Y., T. J. Shankland, and B. T. Poe (2000), Laboratory-based electrical conductivity in the Earth's mantle, *Journal of Geophysical Research: Solid Earth*, *105*(B12), 27,865–27,875.

Yamazaki, Y., and A. Maute (2017), Sq and EEJ–A review on the daily variation of the geomagnetic field caused by ionospheric dynamo currents, *Space Science Reviews*, *206*(1-4), 299–405.

Yoshino, T., and T. Katsura (2009), Effect of iron content on electrical conductivity of ringwoodite, with implications for electrical structure in the transition zone, *Physics of the Earth and Planetary Interiors*, *174*(1), 3–9.

Yoshino, T., and T. Katsura (2012), Re-evaluation of electrical conductivity of anhydrous and hydrous wadsleyite, *Earth and Planetary Science Letters*, *337*, 56–67.

Yoshino, T., M. Nishi, T. Matsuzaki, D. Yamazaki, and T. Katsura (2008a), Electrical conductivity of majorite garnet and its implications for electrical structure in the mantle transition zone, *Physics of the Earth and Planetary Interiors*, *170*(3), 193–200.

Yoshino, T., G. Manthilake, T. Matsuzaki, and T. Katsura (2008b), Dry mantle transition zone inferred from the conductivity of wadsleyite and ringwoodite, *Nature*, *451*(7176), 326–329.

554 Yoshino, T., E. Ito, T. Katsura, D. Yamazaki, S. Shan, X. Guo, M. Nishi, Y. Higo, and K.-i. Funakoshi
555 (2011), Effect of iron content on electrical conductivity of ferropericlase with implications for the
556 spin transition pressure, *Journal of Geophysical Research: Solid Earth*, *116*(B4).
557 Yoshino, T., A. Shimojuku, S. Shan, X. Guo, D. Yamazaki, E. Ito, Y. Higo, and K.-i. Funakoshi
558 (2012), Effect of temperature, pressure and iron content on the electrical conductivity of olivine
559 and its high-pressure polymorphs, *Journal of Geophysical Research: Solid Earth*, *117*(B8).
560 Yoshino, T., S. Kamada, C. Zhao, E. Ohtani, and N. Hirao (2016), Electrical conductivity model of
561 Al-bearing bridgmanite with implications for the electrical structure of the Earth's lower mantle,
562 *Earth and Planetary Science Letters*, *434*, 208–219.
563 Zhang, B., T. Yoshino, X. Wu, T. Matsuzaki, S. Shan, and T. Katsura (2012), Electrical conductivity
564 of enstatite as a function of water content: implications for the electrical structure in the upper
565 mantle, *Earth and Planetary Science Letters*, *357*, 11–20.
566 Zhao, C., and T. Yoshino (2016), Electrical conductivity of mantle clinopyroxene as a function of
567 water content and its implication on electrical structure of uppermost mantle, *Earth and Planetary*
568 *Science Letters*, *447*, 1–9.
569 Zhu, H., E. Bozdağ, and J. Tromp (2015), Seismic structure of the European upper mantle based on
570 adjoint tomography, *Geophysical Journal International*, *201*(1), 18–52.

Supporting Information for "Joint inversion of daily and long-period geomagnetic variations reveals lateral variations in upper mantle and transition zone water content"

F. D. Munch[1], **A. V. Grayver**[1], **M. Guzavina**[1], **A. V. Kuvshinov**[1], **A. Khan**[1,2]

[1]Institute of Geophysics, ETH Zurich, Switzerland
[2]Institute of Theoretical Physics, University of Zurich, Switzerland

Content

1. Figures S1 to S9
2. Captions to figures S1 to S9
3. Table S1
4. Caption to table S1

Introduction

Figure S1 summarizes the distribution of permanent geomagnetic observatories used in the source coefficient estimation procedure described in Appendix A. Figure S2 depicts times series of coefficient of determination obtained assuming different set of spherical harmonics coefficients to describe the magnetospheric ring current. We find significant differences in the estimated coefficients of determination for 8, 10, and 13 source coefficients, while only marginal changes are observed when 15 coefficients are used.

Our scheme to estimate of source coefficients requires a priori Earth's conductivity model which consists of a mantle with 1-D conductivity distribution overlaid by a surface layer of known laterally-variable conductance. Figure S3 depicts examples of transfer functions obtained when two different 1-D mantle conductivity profiles are used for the source coefficient estimation. We find that differences in the estimated transfer functions are within experimental uncertainties.

The estimated transfer functions were individually inverted to retrieve the most probable set of conductivity models underneath 20 geomagnetic observatories. Station geographic locations and acronyms are depicted in Figure S4 and detailed in Table S1. Figure S5 illustrates the posterior probability distributions retrieved when inverting daily and long-period signals separately and jointly at a single station (Alice Spring in Australia).

Finally, Figures S6–S8 summarize the quality of the data fit for each geomagnetic observatory considered in this study. Figure S9 shows sampled electrical conductivity profiles retrieved from the joint inversion of ionospheric and magnetospheric transfer functions and best-fitting laboratory-based conductivity profiles for Yoshino-Katsura (YK) database.

Corresponding author: Federico D. Munch, federico.munch@erdw.ethz.ch

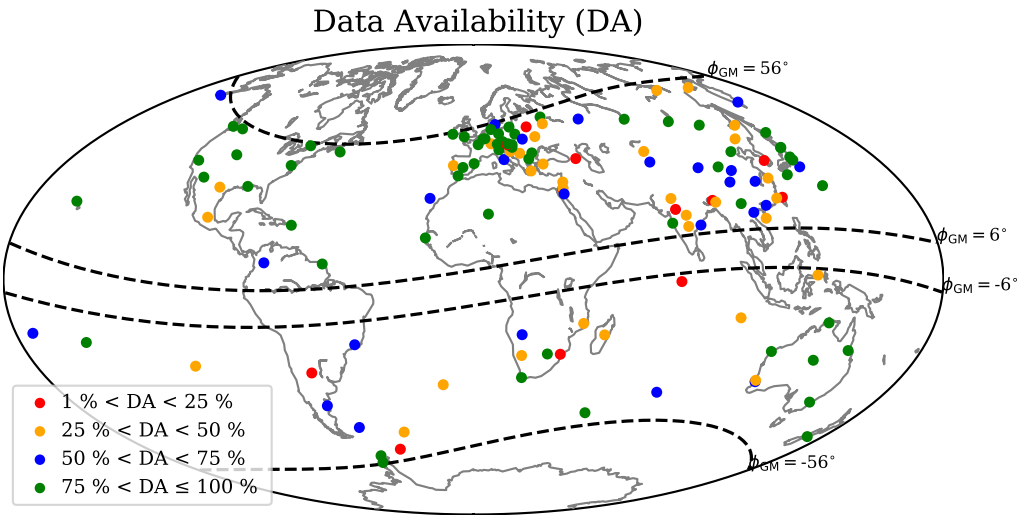

Figure S1. Distribution of permanent observatories (geomagnetic latitudes between ±6° and ±55°, shown in figure by dashed lines) used for source coefficient estimation (Section 2.1) color-coded by data availability (DA). DA equal to 100% corresponds to 20 years of data.

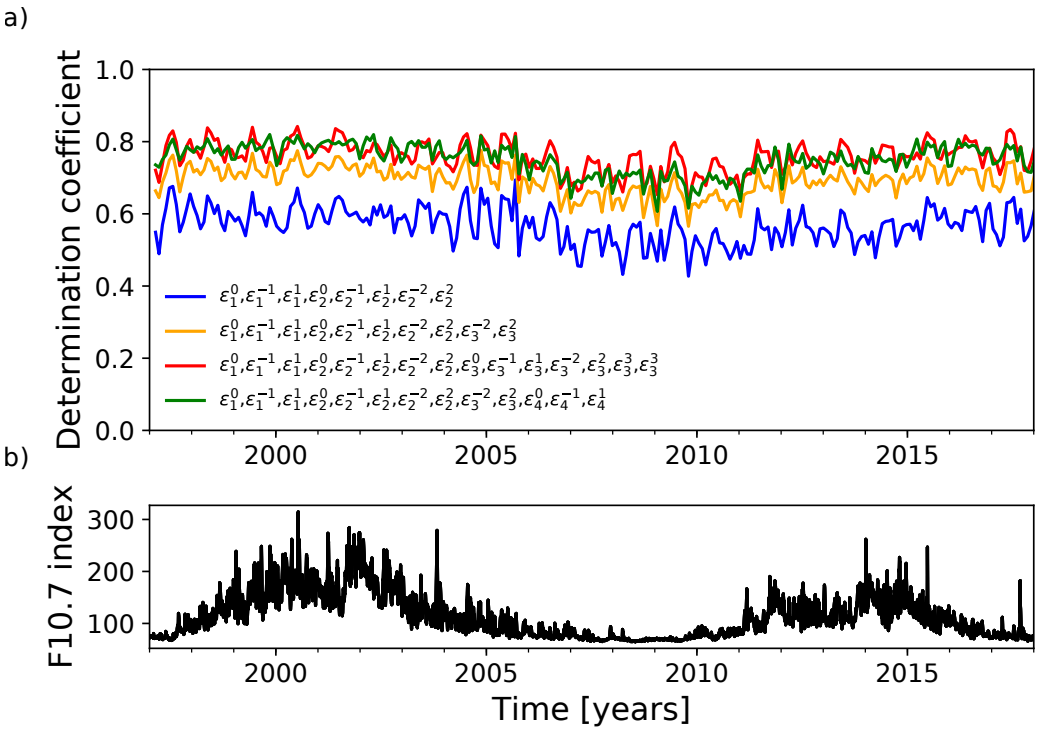

Figure S2. (a) Coefficients of determination obtained using different sets of spherical harmonic (SH) coefficients to describe the magnetospheric ring current. (b) Time series of F10.7 index (extracted from http://lasp.colorado.edu/lisird/data/noaa_radio_flux/), which is a proxy for solar activity. We find a good correlation between the coefficients of determination and F10.7 index reflecting that magnetospheric source is stronger during magnetically-active years.

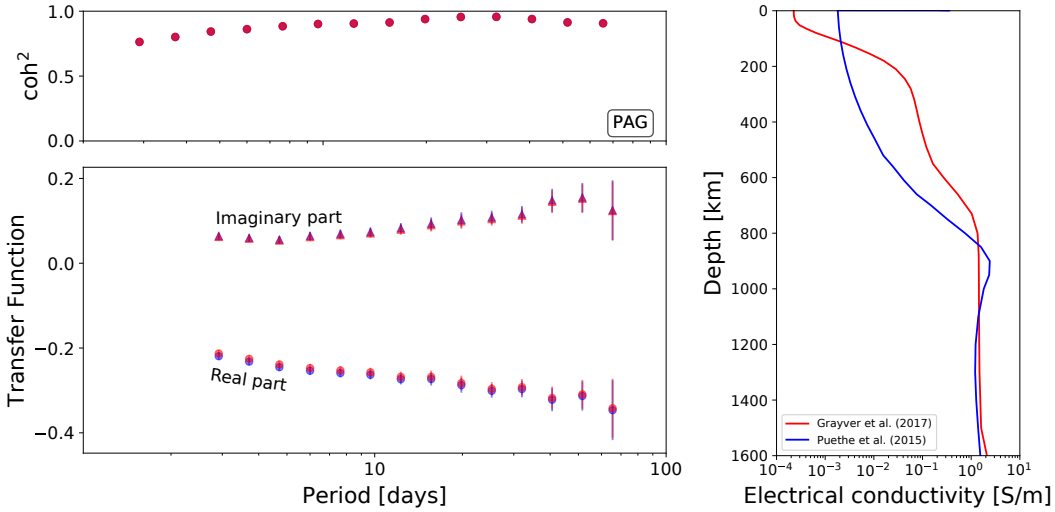

Figure S3. Left: Squared coherencies (top) and real (circles) and imaginary (triangles) parts of the transfer functions (bottom) obtained when two different mantle 1-D conductivity profiles (shown in the right plot) were used for the source coefficients estimation. The results are for the observatory Panagyurishte (PAG). Differences in the estimated transfer functions are within observed uncertainties.

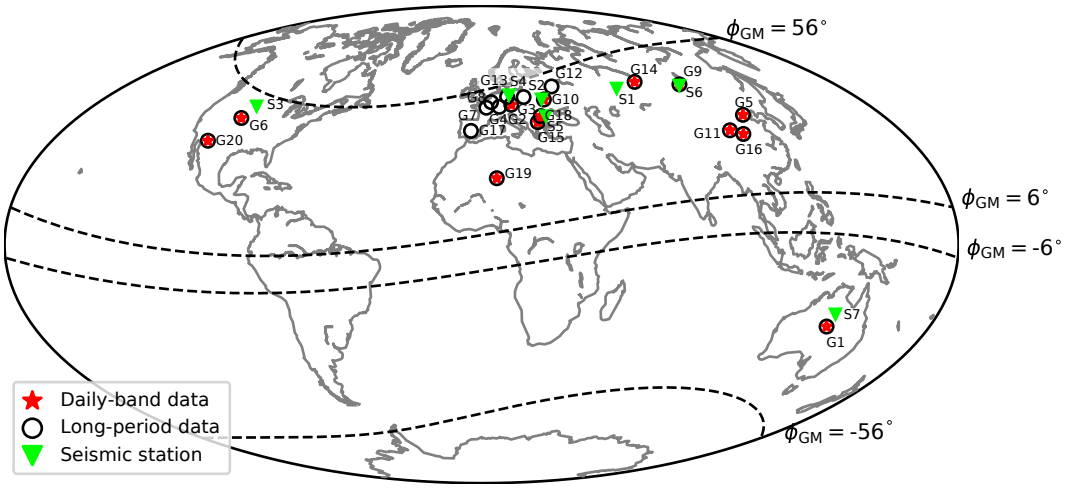

Figure S4. Geographic location of mid-latitude observatories (geomagnetic latitudes φ_{GM} between ±6° and ±56°) used in this study. Red stars and black circles denote stations at which the observed daily and long-period transfer functions are successfully fitted in the inversion, respectively. Green triangles indicate seismic stations for which constraints on mantle temperature and composition were derived by *Munch et al.* [2019] from analysis of short- and long-period seismic data. Station information is summarized in Table S1. Data fit for all stations are shown in Figures S6–S8.

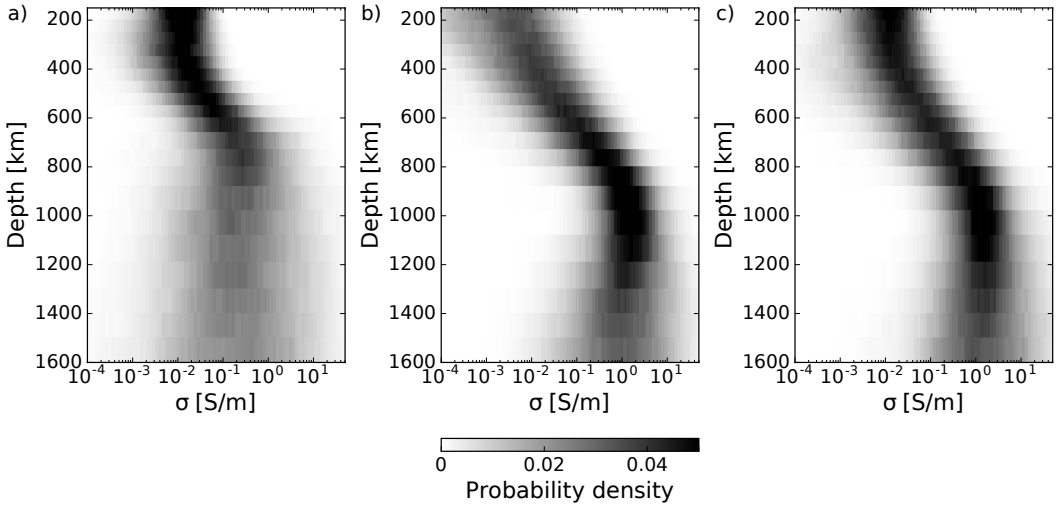

Figure S5. Posterior probability distributions for Alice Springs geomagnetic observatory (G1 station in Figure S4) obtained from the inversion of (a) daily transfer functions (TFs), (b) long-period TFs, and (c) daily and long-period TFs, with black indicating most probable and white least probable conductivity models. The posterior probability distributions were determined by computing a histogram of inferred conductivities for each layer assuming a bin-size of 0.05 on the log scale.

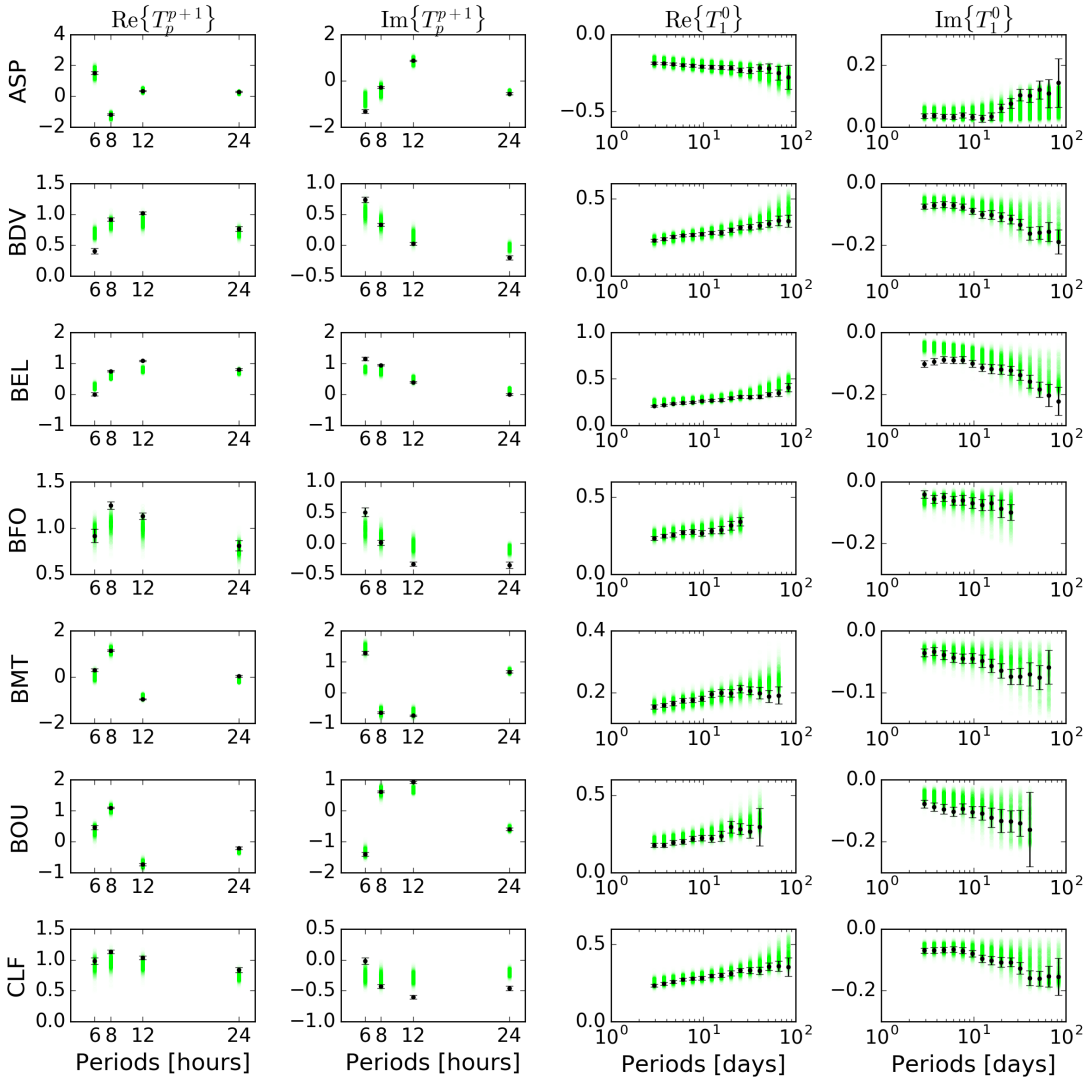

Figure S6. Real (Re) and Imaginary (Im) parts of the observed (black) and modelled (green) ionospheric (6–24 hours; left) and magnetospheric (3–85 days; right) transfer functions for Alice Springs (ASP), Budkov (BDV), Belsk (BEL), Black Forest (BFO), Beijing Ming Tombs (BMT), Boulder (BOU), and Chambon la Foret (CLF) geomagnetic observatories. Uncertainties of the observed transfer functions are indicated by the error bars. p runs 1,2, 3 and 4 when period runs 24, 12, 8 and 6 hours respectively.

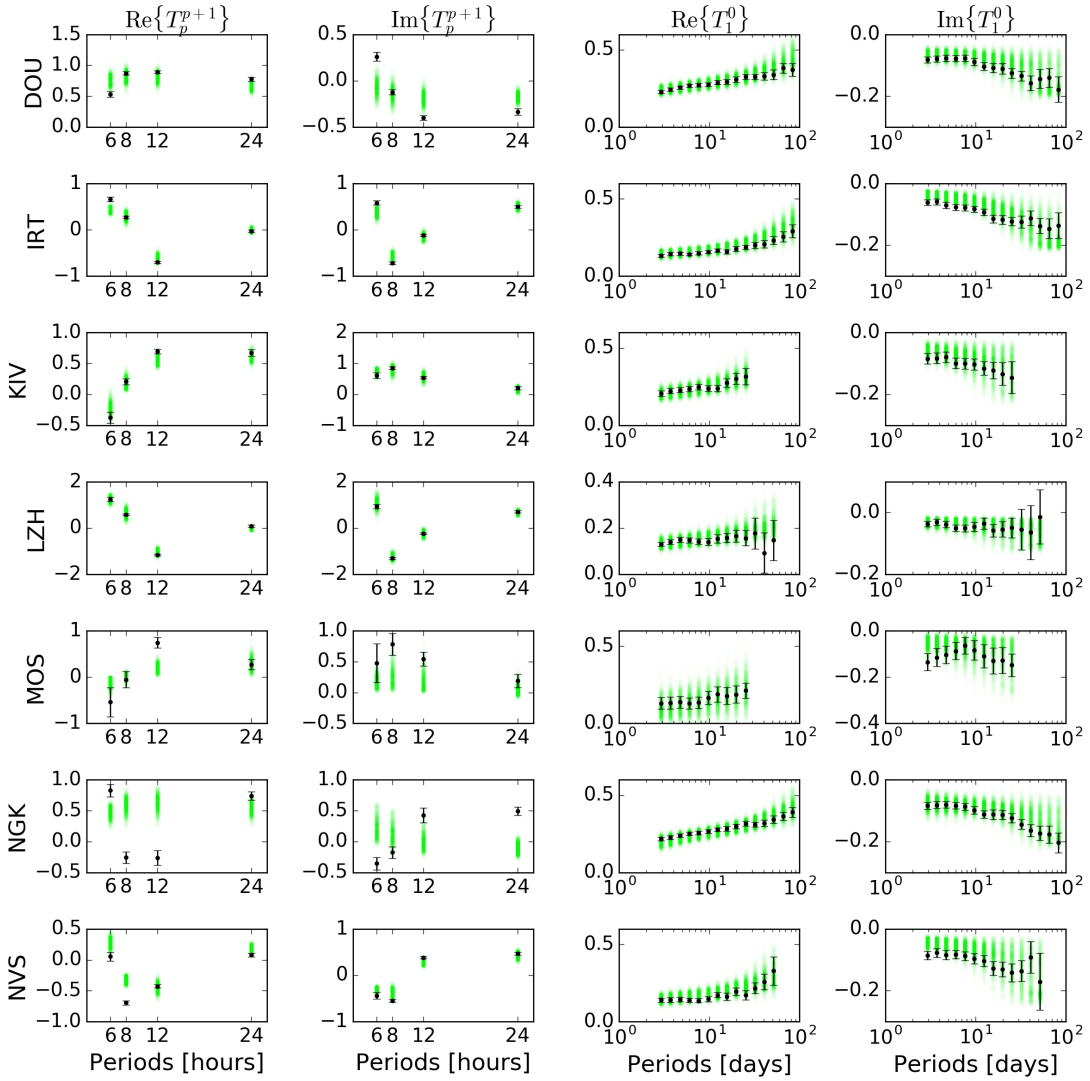

Figure S7. Real (Re) and Imaginary (Im) parts of the observed (black) and modelled (green) ionospheric (6–24 hours) and magnetospheric (3–85 days) transfer functions for Dourbes (DOU), Irkutsk (IRT), Kiev (KIV), Lanzhou (LZH), Moscow (MOS), Niemegk (NGK), and Novosibirsk (NVS) geomagnetic observatories. Uncertainties of the observed transfer functions are indicated by the error bars. p runs 1,2, 3 and 4 when period runs 24, 12, 8 and 6 hours respectively.

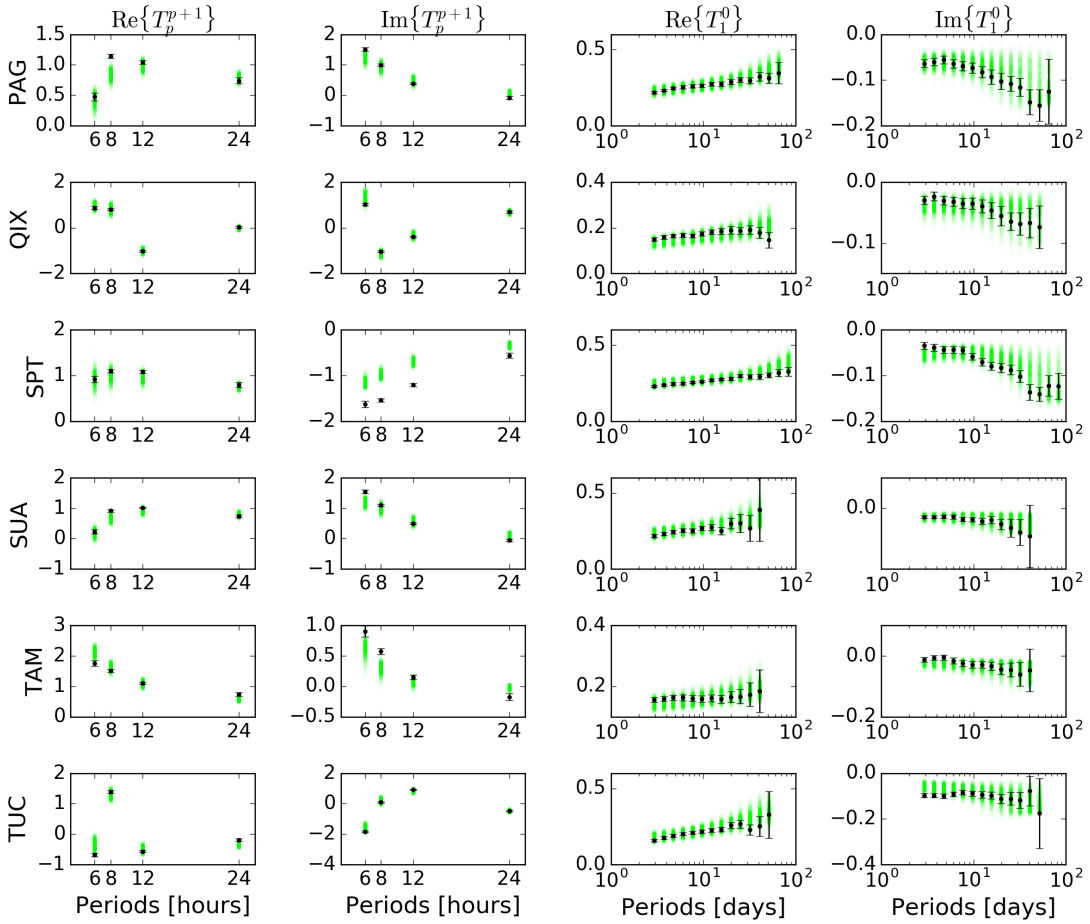

Figure S8. Real (Re) and Imaginary (Im) parts of the observed (black) and modelled (green) ionospheric (6–24 hours) and magnetospheric (3–85 days) transfer functions for Panagjurishte (PAG), Qianling (QIX), San Pablo-Toledo (SPT), Surlari (SUA), Tamanrasset (TAM), and Tucson (TUC) geomagnetic observatories. Uncertainties of the observed transfer functions are indicated by the error bars. p runs 1,2, 3 and 4 when period runs 24, 12, 8 and 6 hours respectively.

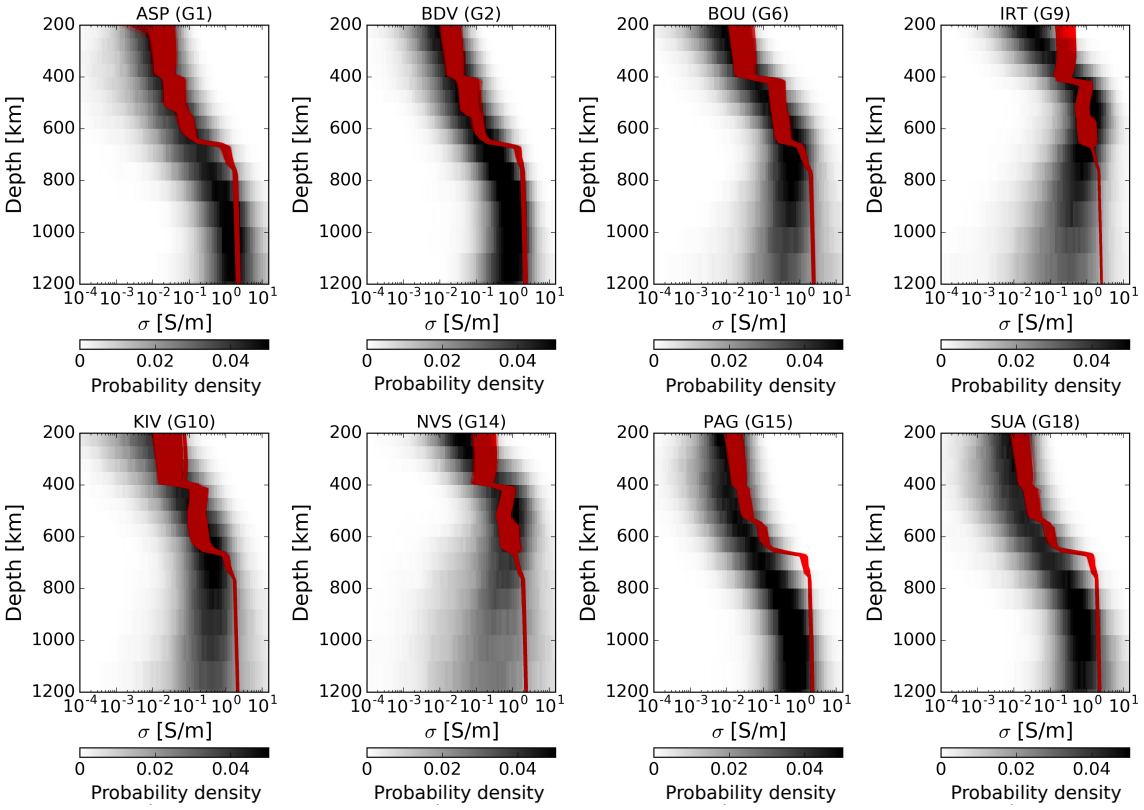

Figure S9. Posterior probability density of electrical conductivity (σ) retrieved from the joint inversion of ionospheric and magnetospheric transfer functions (black) and best-fitting laboratory-based conductivity profiles (red) for YK database. Geographic location of each geomagnetic observatory are shown in Figure 2 and stations acronym are defined in Table 2.

Code	Acronym	Name	Lat. [°]	Lon. [°]
G1	ASP	Alice Springs	-23.62	133.88
G2	BDV	Budkov	48.89	14.02
G3	BEL	Belsk	51.65	20.80
G4	BFO	Black Forest	48.14	8.32
G5	BMT	Beijing Ming Tombs	40.11	116.20
G6	BOU	Boulder	39.94	-105.23
G7	CLF	Chambon la Foret	47.83	2.27
G8	DOU	Dourbes	49.91	4.60
G9	IRT	Irkutsk	51.98	104.45
G10	KIV	Kiev	50.53	30.30
G11	LZH	Lanzhou	35.90	103.85
G12	MOS	Moscow	55.29	37.32
G13	NGK	Niemegk	51.88	12.68
G14	NVS	Novosibirsk	54.67	83.23
G15	PAG	Panagjurishte	42.33	24.18
G16	QIX	Qianling	34.37	108.20
G17	SPT	San Pablo-Toledo	39.36	-4.35
G18	SUA	Surlari	44.49	26.25
G19	TAM	Tamanrasset	22.66	5.53
G20	TUC	Tucson	31.99	-110.73
S1	BRVK	Borovoye	53.06	70.28
S2	KIEV	Kiev	50.70	29.22
S3	RSSD	Black Hills	44.12	-104.04
S4	RUE	Ruedersdorf	52.48	13.78
S5	TIRR	Tirgusor	44.46	28.41
S6	TLY	Talaya	51.68	103.64
S7	WRAB	Tennant Creek	-19.93	134.40

Table S1. Summary of geomagnetic observatory (G) and seismic station (S) codes, acronyms, names, geographic latitudes, and longitudes.

References

Munch, F., A. Khan, B. Tauzin, M. van Driel, and D. Giardini (2019), Seismological evidence for the existence of thermo-chemical heterogeneity in Earth's continental mantle, *manuscript under consideration for publication in Nature Geoscience*.